Pursuant to the DOE Public Access Plan, this document represents the authors' peer-reviewed, accepted manuscript.
The published version of the article is available from the relevant publisher.

ACS NANO

www.acsnano.org

ARTICLE

3D Detection of Lithiation and Lithium Plating in Graphite Anodes during Fast Charging

Alec S. Ho, Dilworth Y. Parkinson, Donal P. Finegan, Stephen E. Trask, Andrew N. Jansen, Wei Tong, and Nitash P. Balsara*

Cite This: https://doi.org/10.1021/acsnano.1c02942

Read Online

ACCESS | Metrics & More | Article Recommendations

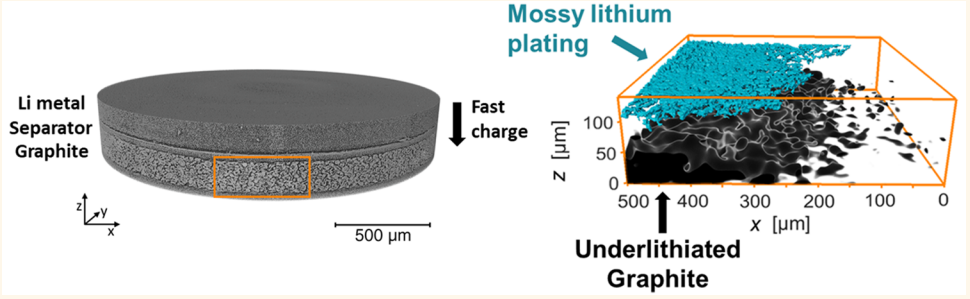

ABSTRACT: **A barrier to the widespread adoption of electric vehicles is enabling fast charging lithium-ion batteries. At normal charging rates, lithium ions intercalate into the graphite electrode. At high charging rates, lithiation is inhomogeneous, and metallic lithium can plate on the graphite particles, reducing capacity and causing safety concerns. We have built a cell for conducting high-resolution *in situ* X-ray microtomography experiments to quantify three-dimensional lithiation inhomogeneity and lithium plating. Our studies reveal an unexpected correlation between these two phenomena. During fast charging, a layer of mossy lithium metal plates at the graphite electrode−separator interface. The transport bottlenecks resulting from this layer lead to underlithiated graphite particles well-removed from the separator, near the current collector. These underlithiated particles lie directly underneath the mossy lithium, suggesting that lithium plating inhibits further lithiation of the underlying electrode.**

KEYWORDS: *lithium plating, fast charging, lithium-ion battery, heterogeneity, X-ray tomography, DVC*

Fast charging lithium-ion batteries would help enable the widespread adoption of electric vehicles.[1] Thus, it is not surprising that numerous researchers are examining the effect of charging rate on both performance at the battery level and redox reaction kinetics at the molecular level.[2−5] Under normal charging conditions, lithium fills in between the carbon layers within the graphitic anode in a series of stages, ultimately resulting in the formation of LiC_6 upon full lithiation. Under fast charging conditions, however, lithium plates on the graphite particles, causing a loss of capacity and introducing a significant safety hazard.[6,7] In spite of considerable efforts, many questions concerning lithium plating and its effect on other parts of the electrode remain unresolved.

Electrodes in lithium-ion batteries are complex three-dimensional (3D) structures made up of redox-active particles surrounded by pores that are filled with a liquid electrolyte. Even under extremely slow charging conditions, the lithiation of graphite electrodes is not uniform.[8] Lithium concentration gradients in both the liquid electrolyte and the solid-phase active materials occur, which lead to more rapid lithiation of graphite particles near the separator and low rates of lithiation near the current collector.[9,10] The pathways that lithium ions must navigate as they reach deep into the electrode are tortuous. It is possible that pathways surrounding some of the particles are more tortuous than others. We thus expect inhomogeneous lithiation not only in the through-plane direction but even within a plane at a fixed distance, *z*, from the current collector. Minimizing inhomogeneous lithium intercalation is much more difficult at high charging

Received: April 7, 2021
Accepted: June 7, 2021

Downloaded via NATL RENEWABLE ENERGY LABORATORY on June 14, 2021 at 22:30:57 (UTC).
See https://pubs.acs.org/sharingguidelines for options on how to legitimately share published articles.

© XXXX American Chemical Society

Pursuant to the DOE Public Access Plan, this document represents the authors' peer-reviewed, accepted manuscript.
The published version of the article is available from the relevant publisher.

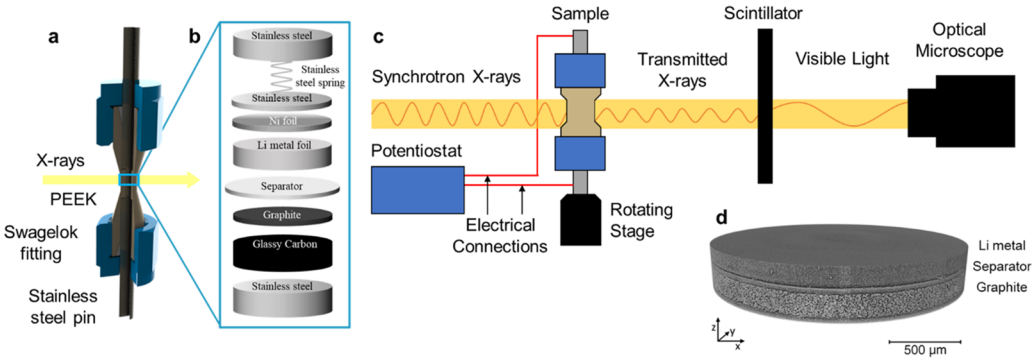

Figure 1. Schematics of (a) polyether ether ketone (PEEK) cell holder, (b) encased cell, and (c) experimental beamline setup of *in situ* X-ray microtomography. (d) Volume rendering of a portion of a pristine lithium-graphite cell.

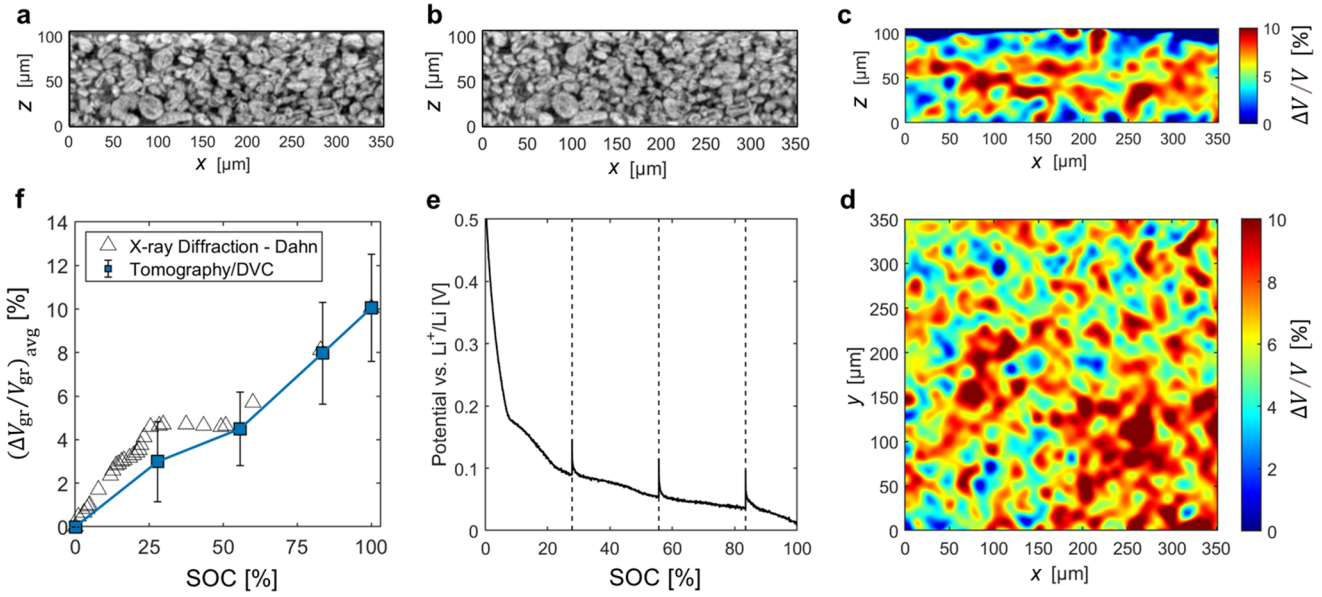

Figure 2. Cross-sectional slice in the *xz*-plane of the graphite composite electrode in an X-ray tomogram of a cell (a) before and (b) after C/10 lithiation to 100% state-of-charge (SOC). The graphite particles are bright gray and the darker gray space in between is filled with electrolyte and the inactive components of the composite electrode. Volumetric strain, $\Delta V/V$, contour map result from digital volume correlation (DVC) between the volume sets before and after C/10 lithiation to 100% SOC taken from the (c) y = 200 μm cross-sectional slice in the *xz*-plane and (d) z = 55 μm top view slice in the *xy*-plane. (e) Lithiation profile of a lithium-graphite cell during *in situ* X-ray tomography. Dashed lines indicate when lithiation was paused for tomogram acquisition. (f) Average volumetric expansion of the graphite, $(\Delta V_{gr}/V_{gr})_{avg}$, as a function of SOC. Open triangles give the expansion based on X-ray diffraction results by Dahn.[36,37] Blue squares show the expansion calculated from the DVC strain map. The blue lines through the DVC data give the calibration for converting from strain to SOC.

rates.[11,12] In this paper, we study lithium plating in a rapidly charged graphite electrode. Lithium plating at one value of z of the cell can, in principle, affect lithium intercalation at other values of z. Our objective is to study this effect.

While the interplay between lithium plating and lithium intercalation in a composite graphite electrode can be studied indirectly using charge/discharge characteristics or post mortem analysis,[13,14] we focus on *in situ* characterization. A wide variety of *in situ* and *operando* techniques, including optical microscopy,[15,16] nuclear magnetic resonance,[17] electron paramagnetic resonance,[18] neutron and X-ray diffraction,[10,19] and measuring voltage relaxation[20,21] have been used to detect lithium plating. However, all of these techniques are limited to one or two dimensions. For example, the distance between graphene layers increases during lithiation, and this can be followed *in situ* by X-ray diffraction (XRD). Since the crystal structures of metallic lithium and graphite (lithiated or unlithiated) are distinct, these processes can be followed either laterally or as a function of z in separate experiments. Since XRD requires the beam to pass through all material in its line of sight before reaching the detector, probing an electrode in the z direction necessarily averages information along the plane of sight (*xy*-plane). Similarly, probing an electrode at positions on the *xy*-plane averages information along the z direction.

In this study, we track both lithium plating and lithium intercalation as a function of x, y, and z in a graphite electrode using *in situ* hard X-ray microtomography. Our approach is built on the work of Pietsch et al.[22] and Finegan et al.,[23] who used digital volume correlation (DVC) to analyze X-ray tomography data. X-ray microtomography is a noninvasive technique that can yield spatial information about materials in three dimensions,[24−31] but image noise and the low attenuation coefficient of lithium and carbon have limited its application in studying lithium plating on graphite.[32] We have addressed this limitation by building an *in situ* cell that

https://doi.org/10.1021/acsnano.1c02942
ACS Nano XXXX, XXX, XXX−XXX

Pursuant to the DOE Public Access Plan, this document represents the authors' peer-reviewed, accepted manuscript.
The published version of the article is available from the relevant publisher.

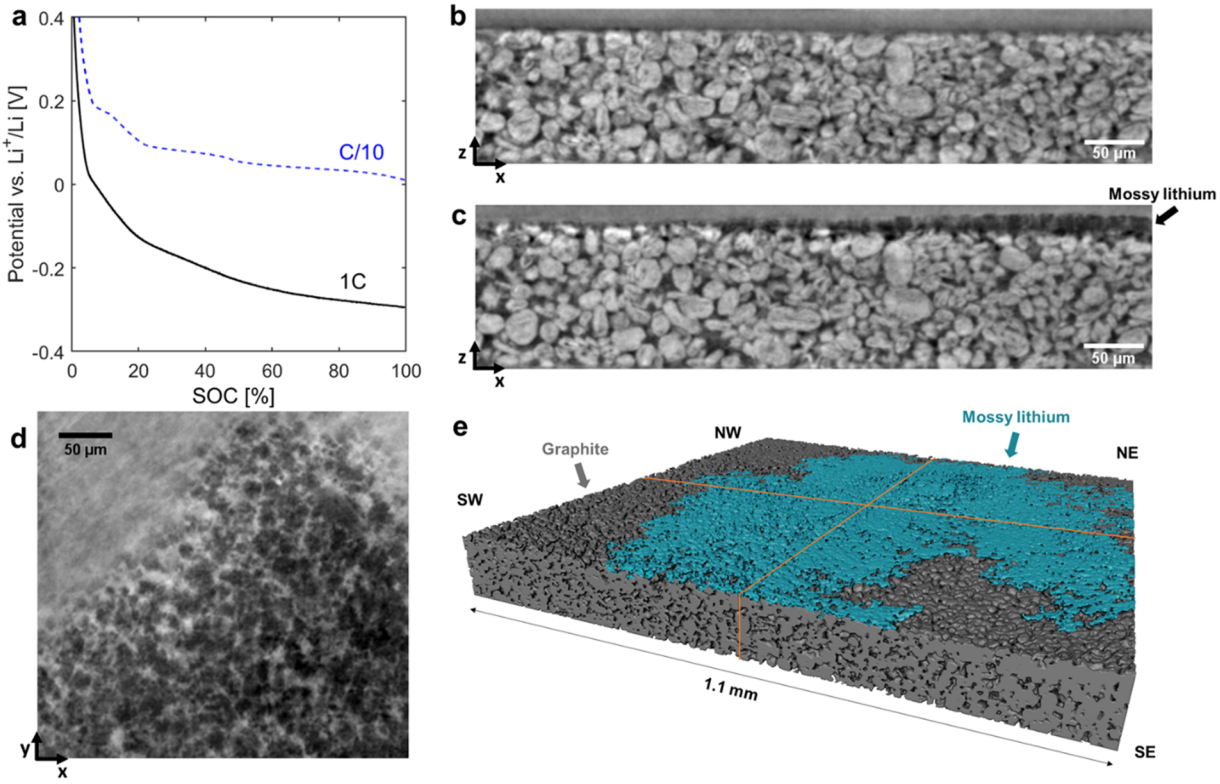

Figure 3. (a) Lithiation profiles of the lithium−graphite cell at a C/10 lithiation rate during formation (blue dotted line), and a 1C lithiation rate during *in situ* X-ray tomography (solid black line). Cross-sectional slice in the *xz*-plane of a graphite electrode in an X-ray tomogram of a cell (b) before and (c) after 1C lithiation to 100% state-of-charge (SOC). Mossy lithium forms on the graphite surface at the electrode-separator interface and appears black-gray in (c). (d) Top view of a portion of the mossy lithium in the *xy*-plane. The mossy lithium consists of interconnected pebbles with electrolyte in the gaps and pores. (e) Volume rendering of the segmented graphite electrode after 1C intercalation to 100% SOC. The graphite is shown in gray, and the mossy lithium is shown in turquoise. The added orange lines divide the electrode into quadrants designated as NW, NE, SW, and SE. For ease of computation, this study focuses on the NW region.

facilitates retrieval of sharp images with good contrast between phases, yielding high-resolution tomograms where graphite, pore, and lithium metal phases can be distinguished. We demonstrate that inhomogeneous lithium plating near the separator influences the uneven lithium intercalation in graphite particles well-removed from the location of plated lithium.

RESULTS AND DISCUSSION

The X-ray microtomography setup and cell configuration used in this study are described in detail in the Experimental Section and are shown in Figure 1. An airtight *in situ* cell holder compatible with X-rays (Figure 1a) housed a lithium−metal−graphite cell (Figure 1b). The experimental setup for X-ray tomography is shown in Figure 1c, and the tomography data are used to reconstruct the 3D morphology of the cell. A volume rendering of this cell with the two electrodes and the separator thus obtained is shown in Figure 1d. While our setup enables imaging of both electrodes as a function of state-of-charge (SOC), we focus on changes in the graphite electrode.

Parts a and b of Figure 2 show 2D images of a graphite electrode in a cell taken from the same cross-sectional slice through the tomogram before lithiation and after lithiation at a slow rate of C/10. The graphite particles appear gray, while the electrolyte-filled pores appear dark gray in the images. To a good approximation, the same particles can be seen in approximately the same locations in the two figures. The lithiation was stopped when the number of coulombs passed measured by the potentiostat matched the capacity of the graphite electrode. The nominal state-of-charge of this electrode is thus 100%. Relative to the unlithiated state, graphite particles expand in the positive z direction (toward the separator) as well as in both the positive x and y directions.

Tomograms were analyzed using digital volume correlation (DVC).[33,34] The resulting 3D displacement fields were used to calculate 3D volumetric strain fields using eqs 1 and 2

$$\varepsilon_{ij} = \frac{1}{2}\left[\frac{\partial u_j}{\partial x_i} + \frac{\partial u_i}{\partial x_j}\right] \tag{1}$$

$$\frac{\Delta V}{V} = \varepsilon_{xx} + \varepsilon_{yy} + \varepsilon_{zz} \tag{2}$$

where ε_{ij} is the strain tensor for small deformations, $\partial u_j/\partial x_i$ is the displacement gradient of the u_j component of the displacement field in the x_i direction, and $\Delta V/V$ is the volumetric strain, which is composed of the normal strains (i = x, y, or z). The displacements in eq 1 are calculated from a tomogram of a lithiated electrode with respect to a tomogram of the same unlithiated electrode.

Figure 2c shows the volumetric strain field calculated from DVC displacement fields using eqs 1 and 2 for the slices shown in Figures 2a,b. Differences in volumetric strains are seen at various locations across this slice. In the interior of the electrode, most of the voxels exhibit volumetric strains between 5 and 10%. A few voxels exhibit strains as high as

https://doi.org/10.1021/acsnano.1c02942
ACS Nano XXXX, XXX, XXX−XXX

Pursuant to the DOE Public Access Plan, this document represents the authors' peer-reviewed, accepted manuscript.
The published version of the article is available from the relevant publisher.

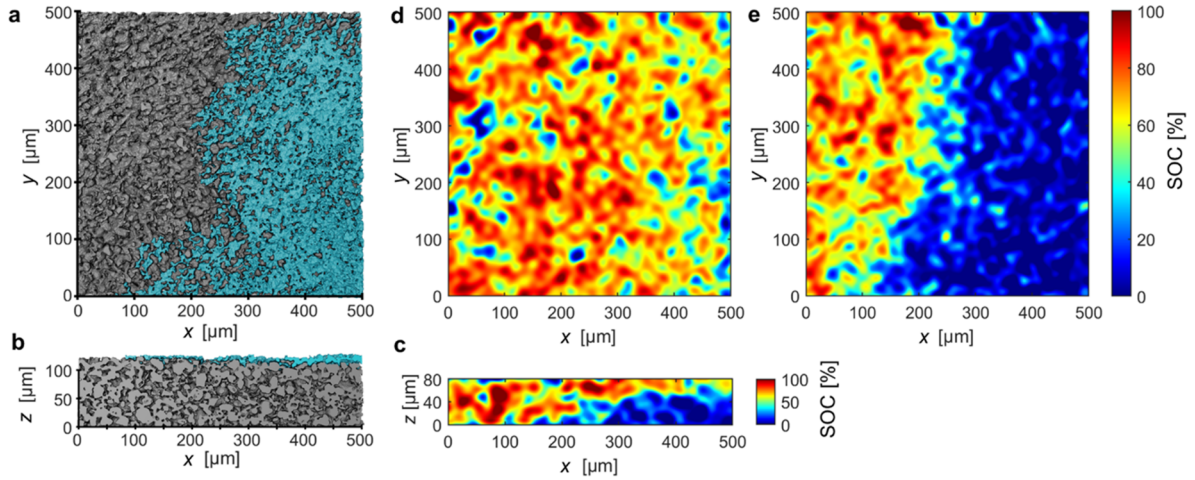

Figure 4. Volume rendering of the NW portion of the segmented graphite electrode in the (a) *xy*-plane and (b) *xz*-plane after 1C intercalation to 100% state-of-charge (SOC). The graphite is shown in gray, and the mossy lithium is shown in turquoise. SOC contour map of the same portion of the graphite electrode from the slice (c) $y = 250\ \mu$m in the *xz*-plane, (d) $z = 70\ \mu$m in the *xy*-plane, and (e) $z = 20\ \mu$m in the *xy*-plane. Digital volume correlation was used to generate volumetric strain maps, which were converted to SOC using the calibration curve in Figure 2f. We observe a lithium "shadow effect", where poor lithiation occurs at the back of the graphite in the region underneath the region of lithium plating.

12%; note the darkest red voxels in Figure 2c. A recent study suggested that bulk graphite expands by 13% upon lithiation.[35] Figure 2d shows an orthogonal slice in the *xy* plane at $z = 55$ μm. The range of volumetric strains seen in this slice is similar to that of Figure 2c. We see generally homogeneous expansion across the graphite electrode. Of course, expansion is not perfectly homogeneous, as evidenced by the presence of different values of $\Delta V/V$ at different locations of the cell (Figure 2c,d). The length scale of the regions of high (red) and low (blue) strain are similar to the length scale of the particles; compare Figures 2b,c.

The composite graphite electrode contains particles that expand upon lithiation and other components, namely the binder, conductive additive, and electrolyte, that do not change in volume. Our DVC results reflect the average strain of the composite electrode, which we write as

$$\boldsymbol{\varepsilon} = \phi_{\mathrm{gr}}\boldsymbol{\varepsilon}^{(\mathrm{gr})} + \phi_{\mathrm{inactive}}\boldsymbol{\varepsilon}^{(\mathrm{inactive})} \tag{3}$$

where ϕ_{gr} and $\boldsymbol{\varepsilon}^{(\mathrm{gr})}$ are the volume fraction and local strain of the active graphite phase and ϕ_{inactive} and $\boldsymbol{\varepsilon}^{(\mathrm{inactive})}$ are the volume fraction and local strain of inactive phases (conductive additive, binder, electrolyte). Assuming the inactive phases contribute negligible strain, eqs 2 and 3 can be combined to give the volumetric strain of the graphite phase, $\Delta V_{\mathrm{gr}}/V_{\mathrm{gr}}$:

$$\frac{\Delta V_{\mathrm{gr}}}{V_{\mathrm{gr}}} = \frac{1}{\phi_{\mathrm{gr}}}\frac{\Delta V}{V} = \frac{1}{\phi_{\mathrm{gr}}}(\varepsilon_{xx} + \varepsilon_{yy} + \varepsilon_{zz}) \tag{4}$$

The parameters in eqs 3 and 4 reflect averages over each voxel.

Figure 2e shows the dependence of the cell potential on SOC during the lithiation process discussed in Figure 2a–d. The dotted lines show intermediate SOCs where lithiation was paused to take a tomogram. The local volumetric strains ($\Delta V/V$) at all SOCs were derived by correlating the tomogram obtained at the SOC of interest to that at 0% SOC. This enables calculation of the local volumetric strain in the graphite phase ($\Delta V_{\mathrm{gr}}/V_{\mathrm{gr}}$). At each SOC, we averaged $\Delta V_{\mathrm{gr}}/V_{\mathrm{gr}}$ over all of the voxels from $z = 0$ to 80 μm to obtain $(\Delta V_{\mathrm{gr}}/V_{\mathrm{gr}})_{\mathrm{avg}}$; we ignore voxels between $z = 80$ and 100 μm, as they are in close proximity to the separator, and this induces artifacts in the DVC calculations. In Figure 2f, we plot $(\Delta V_{\mathrm{gr}}/V_{\mathrm{gr}})_{\mathrm{avg}}$ as a function of SOC. Also shown in Figure 2f is the volumetric expansion of graphite unit cells upon lithiation based on X-ray diffraction (XRD) measurements of the average spacing of carbon layers by Dahn et al.[36,37] At SOC values greater than 50%, we observe quantitative agreement between the tomography-derived volumetric expansion of a composite electrode and XRD. The expansion of graphite upon lithiation is complex, especially at SOC < 50%. One expects different graphite particles to be at different states of charge in a composite electrode. The deviation between the XRD and tomography-derived strains at 28% SOC is not entirely surprising. At SOC values of 84 and 100%, we find quantitative agreement between the average expansion determined by DVC and expansion measured by XRD; note the overlapping triangles and squares. In order to convert the measured local volumetric strain ($\Delta V_{\mathrm{gr}}/V_{\mathrm{gr}}$) to SOC, we use the blue lines through our data as the calibration. When this calibration is used, the few voxels with expansion above 10% give SOC values greater than 100%. We certainly do not expect SOC values to exceed 100%. Given that some studies suggest that bulk graphite expands by 13% upon lithiation, we could construct a calibration curve that is slightly different from the one we proposed. None of the conclusions presented in this paper would be affected by choice of calibration.

Figure 3a shows the 1C lithiation profile (black solid line) of a second cell during *in situ* X-ray microtomography. The applied overpotential goes well below the Li/Li$^+$ potential to values as low as −0.3 V, and we thus expect Li$^+$ to plate on the graphite particles. The formation cycle at C/10 just prior to running the tomography experiment at 1C is also shown in Figure 3a. Figure 3b shows a tomographic slice of the unlithiated electrode, while Figure 3c shows the same slice of the lithiated electrode after a 1C charge to 100% SOC; i.e., the charge supplied to the graphite electrode was identical to that supplied during the C/10 formation cycle. The black-gray voxels seen on the right side of the electrode near the electrode-separator interface represent plated lithium; the

https://doi.org/10.1021/acsnano.1c02942
ACS Nano XXXX, XXX, XXX−XXX

Pursuant to the DOE Public Access Plan, this document represents the authors' peer-reviewed, accepted manuscript.
The published version of the article is available from the relevant publisher.

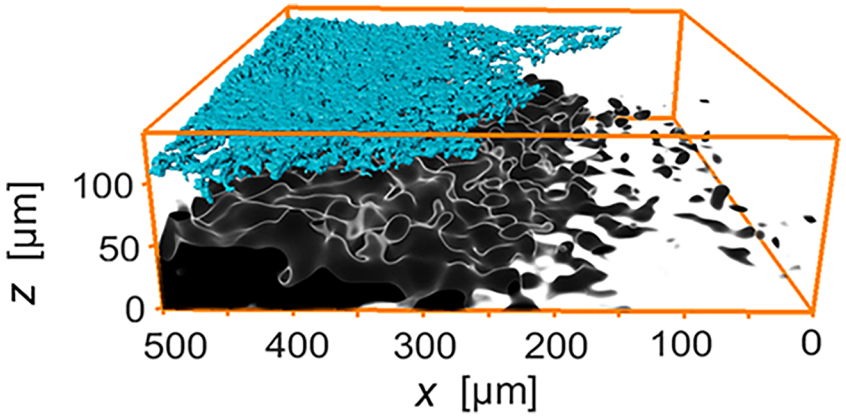

Figure 5. "Shadow effect" in NW portion of graphite electrode after 1C intercalation to 100% state-of-charge (SOC) (rotated 180 deg relative to image in Figure 3e). Volume renderings of segmented lithium plating (turquoise) on graphite where SOC is less than 30% (black). The mossy lithium plating at the top of the electrode impedes lithiation at the back of the electrode, underneath the plating.

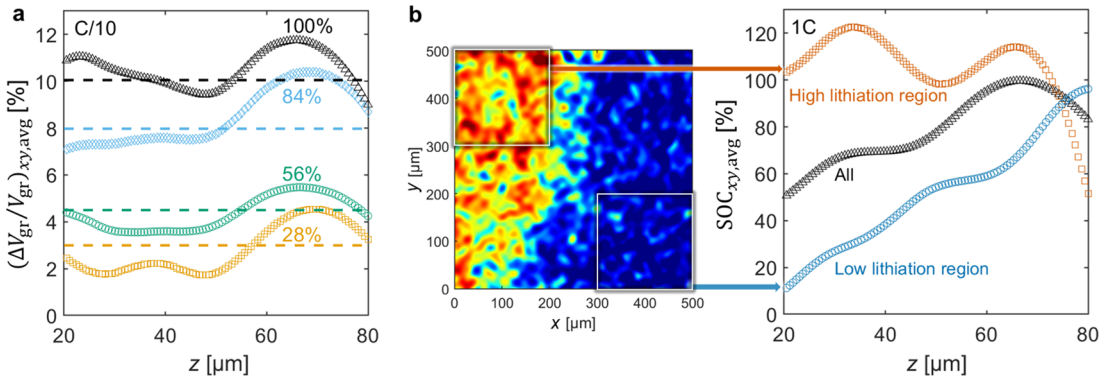

Figure 6. (a) $(\Delta V_{gr}/V_{gr})_{xy,avg}$ strain profiles averaged over the *xy* plane as a function of *z* for strain maps of graphite at SOCs of 28 (yellow squares), 56 (green circles), 84 (blue diamonds), and 100% (black triangles) for the cell in Figure 2. The dotted line gives the average strain across the whole volume for each SOC. The current collector is located at $z = 0$ μm, and the separator is located at $z = 100$ μm. (b) (Left) The SOC in a high lithiation region ($0 \le x \le 200$ μm, $300 \le y \le 500$ μm) and low lithiation region ($300 \le x \le 500$ μm, $0 \le y \le 200$ μm) are sampled for the cell in Figure 4e. (Right) $SOC_{xy,avg}$ profiles averaged over the whole *xy* plane in the NW quadrant (black triangles), the high lithiation region (orange squares), and the low lithiation region (blue circles). The strain profile in the low lithiation region shows a large lithiation gradient.

attenuation coefficient of lithium is lower than that of graphite and thus voxels containing lithium appear darker. Note that such features were not seen upon lithiating at C/10 (see Figure 2). Figure 3d shows a slice in the *xy*-plane that contains plated lithium. The mossy nature of the plated lithium is evident in this image. The black-gray pebbles represent lithium, while the brighter interspersed regions represent the electrolyte. The continuous bright phase near the top left corner represents the separator. It is evident that the plated lithium grows into the separator. Figure 3e shows a volume rendering of the segmented graphite particles (gray) and mossy lithium (turquoise) in a 1.1 mm × 1.1 mm area of the electrode. Due to computational constraints, the DVC analysis was conducted on the northwest (NW) quadrant of this electrode, and the top and side views of this quadrant are presented in parts a and b, respectively, of Figure 4.

Parts c–e of Figure 4 show the SOC maps of the lithiation within the portion of the graphite electrode presented in Figure 4a,b, where volumetric strain is converted to SOC using the calibration in Figure 2f. The SOC in the *xz*-plane of a slice through the middle of the electrode ($y = 250$ μm) is shown in Figure 4c. The current collector is located at $z = 0$ μm and the separator is located at $z = 100$ μm. We again ignore voxels between $z = 80$ and 100 μm, as they are in close proximity to the separator and the region of plated lithium. Since these factors induce artifacts in the DVC calculations, we only show the SOC between $z = 0$ and 80 μm. Charging at 1C clearly leads to inhomogeneous SOC, as evidenced by the blue patch near the current collector from $x = 250$ to 500 μm. Note the absence of such a patch in Figure 2c, where the graphite electrode was charged much more slowly at C/10. Returning to Figure 4, the graphite near the separator ($z = 70$ μm, Figure 4d) lithiates normally and reaches a high SOC. However, a slice of the graphite near the current collector ($z = 20$ μm, Figure 4e) reveals a high SOC region on the left and a low SOC region on the right. The region of poor lithiation lies underneath the region of mossy lithium (Figure 4a), but 50 μm below the separator that is coated with lithium metal. It is clear that the position of the mossy lithium at $z = 100$ μm impedes the transport of lithium ions into graphite particles directly below it near the current collector.

It appears as though lithium plating casts a shadow on the graphite electrode, and we refer to this phenomenon as the "shadow effect". The complex correlations between lithium plating and graphite lithiation are depicted in Figure 5, where we show voxels corresponding to plated lithium and voxels

https://doi.org/10.1021/acsnano.1c02942
ACS Nano XXXX, XXX, XXX–XXX

Pursuant to the DOE Public Access Plan, this document represents the authors' peer-reviewed, accepted manuscript.
The published version of the article is available from the relevant publisher.

corresponding to graphite particles with lithiation less than 30%. To a good approximation, the underlithiated graphite particles lie right below the plated lithium. It is likely that the plated lithium partially blocks the pores that are avenues for transport of lithium to the graphite particles. This blockage reduces the lithium concentration in the electrolytic relative to unblocked portions of the electrode at the same value of z. We posit that the shadow effect occurs because this reduction is so severe that the salt concentration toward the bottom of the electrode beneath the plated lithium is very small.

In Figure 6a we plot the $\Delta V_{gr}/V_{gr}$ strain profiles averaged over the xy-plane, $(\Delta V_{gr}/V_{gr})_{xy,avg}$, as a function of depth, z, at SOCs of 28, 56, 84, and 100% for the C/10 lithiated cell in Figure 2. The dashed lines in the figure represent the global strain average, $(\Delta V_{gr}/V_{gr})_{avg}$, reported in Figure 2f. While the local strains tend to be higher near the separator, strain is a relatively weak function of z. Figure 6b shows the results of xy-averaging as a function of z for the 1C lithiated cell. The values of $(\Delta V_{gr}/V_{gr})_{xy,avg}$ obtained from the DVC analysis were converted to $SOC_{xy,avg}$ using the calibration curve in Figure 2f. We present averages over two squares, one located in the high lithiation region ($0 \le x \le 200$ μm, $300 \le y \le 500$ μm) and one located in the low lithiation region ($300 \le x \le 500$ μm, $0 \le y \le 200$ μm). In the high lithiation region of the 1C cell, the z-dependence of $SOC_{xy,avg}$ determined by our analysis is similar to that obtained at C/10. The calculated SOC values near the electrode-separator interface are likely to be affected by the presence of other phases: the separator and/or plated lithium. Similar effects are expected near the electrode-current collector interface. We therefore focus on the region between $z = 20$ and 80 μm in Figure 6. There is, however, a clear difference seen in the z-dependence of $SOC_{xy,avg}$ in the low lithiation region; $SOC_{xy,avg}$ of the graphite particles near the separator is nearly an order of magnitude greater than the $SOC_{xy,avg}$ of the graphite particles near the current collector. The dependence of $SOC_{xy,avg}$ over the entire electrode area is also shown in Figure 6b. The SOC in the region between $z = 20$ and 50 μm is less than 70%. The average SOC at the end of the 1C charge is 76%. On the basis of our C/10 measurements, the capacity of the graphite electrode examined by DVC (Figure 4) is 12 μAh. This implies that the missing capacity at 1C charge is 2.9 μAh (24% of 12 μAh). If we compute the total volume of voxels corresponding to plated lithium and convert this volume to capacity based on the known density of metallic lithium (0.534 g/cm^3), we obtain 6.2 μAh. If we force agreement between the missing capacity in graphite and the capacity of plated lithium, we would conclude that the plated lithium phase is mossy with a lithium volume fraction of 47%. Characterizing the nanostructure of the mossy lithium is beyond the resolution of our system. Despite this limitation, it is clear that our segmentation and DVC analysis of the *in situ* X-ray tomography results provide a coherent picture of the effect of lithium plating on graphite intercalation.

CONCLUSIONS

In situ X-ray microtomography was performed on graphite electrodes to study the effect of lithium plating on lithium intercalation. The microtomography experiments were used to determine the location of plated lithium by segmentation and the local strain within the graphite electrode by DVC. A strain versus SOC calibration was developed by analyzing tomograms obtained under very slow charging conditions (C/10). Experiments conducted at 1C showed the presence of plated lithium at the electrode-separator interface. One might expect such deposits to introduce transport bottlenecks in composite electrodes. Our surprising finding was that the consequence of these bottlenecks was manifested in underlithiated graphite well-removed from the separator. It appears that plated lithium casts a shadow on the electrode. Our hypothesis is that the transport bottleneck due to plating results in steeper salt concentration gradients within the electrode and that the bottom half of the graphite electrode may be starved of lithium as a consequence. We hope that our study will motivate detailed simulations that probe the effect of lithium plating on the performance of graphite electrodes.

EXPERIMENTAL SECTION

***In Situ* Cell Design and Materials.** To study lithium plating on graphite, cells with lithium metal and graphite electrodes were assembled. The custom cell holder, machined from polyether ether ketone (PEEK), was adapted from Finegan et al.[38] and is shown in Figure 1a. The cell holder was connected to two Swagelok unions with nuts and ferrules on stainless steel current collecting pins to keep the sample airtight. Figure 1b shows a schematic of the encased cell, consisting of a punched 4 mm diameter graphite electrode, 5 mm diameter separator, and 4 mm diameter lithium foil electrode, placed between a glassy carbon rod and a spring-backed stainless steel rod. The graphite electrode consisted of 91.83 wt % Superior Graphite SLC1520P with 2 wt % Timcal C45, 6 wt % Kureha 9300 PVDF Binder, and 0.17 wt % oxalic acid. In its dry state, the coating thickness was 101 on 15 μm copper foil. The coating loading was 13.97 mg cm^{-2} with a density of 1.38 g cm^{-3}, a porosity of 36.2%, and a capacity of approximately 4.8 mAh cm^{-2} based on C/10 formation cycling. C/10 and 1C charging correspond to current densities of 0.48 mA cm^{-2} and 4.8 mA cm^{-2}. The diameters for particle size distribution were D10 = 11 μm, D50 = 17 μm, and D90 = 27 μm. The graphite electrode was soaked in ultrapure water (18.2 MΩ) and a razorblade was used to remove the copper foil backing, followed by drying under active vacuum at 90 °C for at least 48 h. Lithium foil was purchased from Honjo Metals, with a foil thickness of 50 μm. Three layers of lithium metal foil were stacked on top of a piece of nickel foil and then pressed until flat and shiny inside pouch material with a pneumatic press (130 MPa). Cells contained one Celgard 2500 separator and 5 μL 1.2 M lithium hexafluorophosphate (LiPF6) in a 3:7 wt:wt mixture of ethylene carbonate (EC) and ethyl methyl carbonate (EMC).

Cell Operating Conditions. Before exposure to the beam, each cell underwent five formation cycles, where one formation cycle consisted of C/10 graphite intercalation to 0.01 V, 30 min rest, C/5 deintercalation to 1.5 V, and 30 min rest. Formation cycles were performed with a Biologic VMP3 potentiostat, and the cells were placed in a Maccor Temperature Chamber at 25 °C. This cell was used for *in situ* X-ray microtomography, and a portable SP300 potentiostat was used to control the current through the cell in these experiments. Data obtained from the first charge after the formation cycles are discussed in the manuscript.

***In Situ* X-ray Microtomography and Segmentation.** Hard X-ray microtomography was performed at Beamline 8.3.2 at the Advanced Light Source at Lawrence Berkeley National Laboratory. The experimental setup is shown in Figure 1c. Lithium−graphite cells were mounted, imaged, charged to the desired state-of-charge and allowed to rest for 15 min before the next scan. The lithium−graphite cells were imaged at various states-of-charge with a 22 keV monochromatic beam using a 10× lens, resulting in a tomogram with a voxel size of approximately (0.65 μm)^3 and an approximate spatial resolution of 2.0 μm. Approximately 17% of the cell was imaged with this lens configuration. For each tomogram, 1313 images were taken over 180° of rotation with an exposure time of 150−250 ms per image. The total scan time was approximately 10−15 min. The propagation-based phase contrast tomograms were reconstructed using TomoPy's implementation of the Paganin et al. phase retrieval

https://doi.org/10.1021/acsnano.1c02942
ACS Nano XXXX, XXX, XXX−XXX

Pursuant to the DOE Public Access Plan, this document represents the authors' peer-reviewed, accepted manuscript.
The published version of the article is available from the relevant publisher.

algorithm with regularization parameter $\alpha = 0.005$.[39,40] Reconstructed three-dimensional (3D) images were analyzed using the commercially available Avizo software package. To determine the volume fraction of graphite, ϕ_{gr}, in an electrode in the delithiated state, Otsu thresholding was applied to binarize the graphite from the inactive phases, and ϕ_{gr} was determined to be 62.8%. In samples with mossy lithium, the tomographic data was trinarized to identify graphite, mossy lithium, and inactive phases. An anisotropic diffusion filter was applied (20 iterations with time step dt = 20), followed by segmentation with Avizo's Magic Wand tool, which is a region growing algorithm that starts from a seed point and identifies all connected voxels.

Digital Volume Correlation (DVC). Tomograms were cropped to 608 × 608 × 208 voxels and 848 × 848 × 208 voxels for the C/10 and 1C cells, respectively, to isolate regions of interest for input into the DVC algorithm. Fast iterative digital volume correlation (FIDVC)[41] was performed on these volumes. The grid spacing of nodes was 1 voxel and the volume of the correlation window was 32^3 voxels (20.8 μm),[3] which is similar to the D50 particle size of 17 μm. The displacement of each node was estimated by iteratively finding the incremental displacement that maximized the gray-level cross-correlation between the volumes in the correlation window with an image deformation method. The DVC results were further cropped to remove artifacts at the edges of the field of view. The DVC algorithm is designed to calculate strains in bulk materials, not at interfaces. We thus exclude voxels near the current collector or near the separator from our analysis.

AUTHOR INFORMATION

Corresponding Author

Nitash P. Balsara − *Department of Chemical and Biomolecular Engineering, University of California, Berkeley, California 94720, United States; Materials Sciences Division, Lawrence Berkeley National Laboratory, Berkeley, California 94720, United States; Energy Technologies Area, Lawrence Berkeley National Laboratory, Berkeley, California 94720, United States;* orcid.org/0000-0002-0106-5565; Phone: 1-510-642-8973; Email: nbalsara@berkeley.edu

Authors

Alec S. Ho − *Department of Chemical and Biomolecular Engineering, University of California, Berkeley, California 94720, United States; Materials Sciences Division, Lawrence Berkeley National Laboratory, Berkeley, California 94720, United States;* orcid.org/0000-0003-1373-5332

Dilworth Y. Parkinson − *Advanced Light Source, Lawrence Berkeley National Laboratory, Berkeley, California 94720, United States;* orcid.org/0000-0002-1817-0716

Donal P. Finegan − *National Renewable Energy Laboratory, Golden, Colorado 80401, United States;* orcid.org/0000-0003-4633-560X

Stephen E. Trask − *Chemical Sciences and Engineering Division, Argonne National Laboratory, Lemont, Illinois 60439, United States;* orcid.org/0000-0002-0879-4779

Andrew N. Jansen − *Chemical Sciences and Engineering Division, Argonne National Laboratory, Lemont, Illinois 60439, United States*

Wei Tong − *Energy Storage and Distributed Resources Division, Lawrence Berkeley National Laboratory, Berkeley, California 94720, United States*

Complete contact information is available at: https://pubs.acs.org/10.1021/acsnano.1c02942

Notes

The authors declare no competing financial interest.

ACKNOWLEDGMENTS

This work was primarily supported by the Vehicle Technologies Office of the U.S. Department of Energy's Office of Energy Efficiency and Renewable Energy under the guidance of the Advanced Battery Cell Research Program (eXtreme fast charge Cell Evaluation of Lithium-ion batteries, XCEL). A.H. was supported by a National Science Foundation Graduate Research Fellowship DGE-2020294884. Hard X-ray experiments were performed at the Advanced Light Source, which is supported by the Director, Office of Science, Office of Basic Energy Sciences, of the U.S. Department of Energy under Contract No. DE-AC02-05CH11231. D.F. was supported by the Alliance for Sustainable Energy, LLC, the manager and operator of the National Renewable Energy Laboratory for the U.S. Department of Energy (DOE) under Contract No. DE-AC36-08GO28308. A.J. and S.T. were supported by UChicago Argonne, LLC, Operator of Argonne National Laboratory. Argonne National Laboratory is operated under Contract No. DE-AC02-06CH11357. We thank the Cell Analysis, Modeling and Prototyping (CAMP) Facility at Argonne National Laboratory for manufacturing the graphite electrodes. The authors thank E. McShane and Z. Konz for helpful discussions and feedback related to this work.

REFERENCES

(1) Ahmed, S.; Bloom, I.; Jansen, A. N.; Tanim, T.; Dufek, E. J.; Pesaran, A.; Burnham, A.; Carlson, R. B.; Dias, F.; Hardy, K.; Keyser, M.; Kreuzer, C.; Markel, A.; Meintz, A.; Michelbacher, C.; Mohanpurkar, M.; Nelson, P. A.; Robertson, D. C.; Scoffield, D.; Shirk, M.; et al. Enabling Fast Charging − A Battery Technology Gap Assessment. *J. Power Sources* **2017**, *367*, 250−262.

(2) Li, Z.; Huang, J.; Yann Liaw, B.; Metzler, V.; Zhang, J. A Review of Lithium Deposition in Lithium-Ion and Lithium Metal Secondary Batteries. *J. Power Sources* **2014**, *254*, 168−182.

(3) Waldmann, T.; Hogg, B. I.; Wohlfahrt-Mehrens, M. Li Plating as Unwanted Side Reaction in Commercial Li-Ion Cells − A Review. *J. Power Sources* **2018**, *384*, 107−124.

(4) Tomaszewska, A.; Chu, Z.; Feng, X.; O'Kane, S.; Liu, X.; Chen, J.; Ji, C.; Endler, E.; Li, R.; Liu, L.; Li, Y.; Zheng, S.; Vetterlein, S.; Gao, M.; Du, J.; Parkes, M.; Ouyang, M.; Marinescu, M.; Offer, G.; Wu, B. Lithium-Ion Battery Fast Charging: A Review. *eTransportation* **2019**, *1*, 100011.

(5) Bauer, M.; Rieger, B.; Schindler, S.; Keil, P.; Wachtler, M.; Danzer, M. A.; Jossen, A. Multi-Phase Formation Induced by Kinetic Limitations in Graphite-Based Lithium-Ion Cells: Analyzing the Effects on Dilation and Voltage Response. *J. Energy Storage* **2017**, *10*, 1−10.

(6) Goodenough, J. B.; Kim, Y. Challenges for Rechargeable Li Batteries. *Chem. Mater.* **2010**, *22*, 587−603.

(7) Pender, J. P.; Jha, G.; Youn, D. H.; Ziegler, J. M.; Andoni, I.; Choi, E. J.; Heller, A.; Dunn, B. S.; Weiss, P. S.; Penner, R. M.; Mullins, C. B. Electrode Degradation in Lithium-Ion Batteries. *ACS Nano* **2020**, *14*, 1243−1295.

(8) Migge, S.; Sandmann, G.; Rahner, D.; Dietz, H.; Plieth, W. Studying Lithium Intercalation into Graphite Particles *via in Situ* Raman Spectroscopy and Confocal Microscopy. *J. Solid State Electrochem.* **2005**, *9*, 132−137.

(9) Yao, K. P. C.; Okasinski, J. S.; Kalaga, K.; Shkrob, I. A.; Abraham, D. P. Quantifying Lithium Concentration Gradients in the Graphite Electrode of Li-Ion Cells Using: Operando Energy Dispersive X-Ray Diffraction. *Energy Environ. Sci.* **2019**, *12*, 656−665.

(10) Finegan, D.; Quinn, A.; Wragg, D.; Colclasure, A.; Lu, X.; Tan, C.; Heenan, T.; Jervis, R.; Brett, D.; Das, S.; Gao, T.; Cogswell, D.; Bazant, M.; Di Michiel, M.; Checchia, S.; Shearing, P.; Smith, K. Spatial Dynamics of Lithiation and Lithium Plating during High-Rate

Pursuant to the DOE Public Access Plan, this document represents the authors' peer-reviewed, accepted manuscript. The published version of the article is available from the relevant publisher.

Operation of Graphite Electrodes. *Energy Environ. Sci.* **2020**, *13*, 2570−2584.
(11) Colclasure, A. M.; Dunlop, A. R.; Trask, S. E.; Polzin, B. J.; Jansen, A. N.; Smith, K. Requirements for Enabling Extreme Fast Charging of High Energy Density Li-Ion Cells While Avoiding Lithium Plating. *J. Electrochem. Soc.* **2019**, *166*, A1412−A1424.
(12) Colclasure, A. M.; Tanim, T. R.; Jansen, A. N.; Trask, S. E.; Dunlop, A. R.; Polzin, B. J.; Bloom, I.; Robertson, D.; Flores, L.; Evans, M.; Dufek, E. J.; Smith, K. Electrode Scale and Electrolyte Transport Effects on Extreme Fast Charging of Lithium-Ion Cells. *Electrochim. Acta* **2020**, *337*, 135854.
(13) Burns, J. C.; Stevens, D. A.; Dahn, J. R. *In Situ* Detection of Lithium Plating Using High Precision Coulometry. *J. Electrochem. Soc.* **2015**, *162*, A959−A964.
(14) McShane, E. J.; McShane, E. J.; Colclasure, A. M.; Brown, D. E.; Brown, D. E.; Konz, Z. M.; Konz, Z. M.; Smith, K.; McCloskey, B. D. Quantification of Inactive Lithium and Solid-Electrolyte Interphase Species on Graphite Electrodes after Fast Charging. *ACS Energy Lett.* **2020**, *5*, 2045−2051.
(15) Fear, C.; Adhikary, T.; Carter, R.; Mistry, A. N.; Love, C. T.; Mukherjee, P. P. In Operando Detection of the Onset and Mapping of Lithium Plating Regimes during Fast Charging of Lithium-Ion Batteries. *ACS Appl. Mater. Interfaces* **2020**, *12*, 30438−30448.
(16) Gao, T.; Han, Y.; Fraggedakis, D.; Das, S.; Zhou, T.; Yeh, C. N.; Xu, S.; Chueh, W. C.; Li, J.; Bazant, M. Z. Interplay of Lithium Intercalation and Plating on a Single Graphite Particle. *Joule* **2021**, *5*, 393−414.
(17) Matadi, B. P.; Genies, S.; Delaille, A.; Chabrol, C.; de Vito, E.; Bardet, M.; Martin, J.-F.; Daniel, L.; Bultel, Y. Irreversible Capacity Loss of Li-Ion Batteries Cycled at Low Temperature Due to an Untypical Layer Hindering Li Diffusion into Graphite Electrode. *J. Electrochem. Soc.* **2017**, *164*, A2374−A2389.
(18) Wandt, J.; Jakes, P.; Granwehr, J.; Eichel, R. A.; Gasteiger, H. A. Quantitative and Time-Resolved Detection of Lithium Plating on Graphite Anodes in Lithium Ion Batteries. *Mater. Today* **2018**, *21*, 231−240.
(19) Wilhelm, J.; Seidlmayer, S.; Erhard, S.; Hofmann, M.; Gilles, R.; Jossen, A. *In Situ* Neutron Diffraction Study of Lithiation Gradients in Graphite Anodes during Discharge and Relaxation. *J. Electrochem. Soc.* **2018**, *165*, A1846−A1856.
(20) Schindler, S.; Bauer, M.; Petzl, M.; Danzer, M. A. Voltage Relaxation and Impedance Spectroscopy as *in Operando* Methods for the Detection of Lithium Plating on Graphitic Anodes in Commercial Lithium-Ion Cells. *J. Power Sources* **2016**, *304*, 170−180.
(21) Konz, Z. M.; McShane, E. J.; McCloskey, B. D. Detecting the Onset of Lithium Plating and Monitoring Fast Charging Performance with Voltage Relaxation. *ACS Energy Lett.* **2020**, *5*, 1750−1757.
(22) Pietsch, P.; Westhoff, D.; Feinauer, J.; Eller, J.; Marone, F.; Stampanoni, M.; Schmidt, V.; Wood, V. Quantifying Microstructural Dynamics and Electrochemical Activity of Graphite and Silicon-Graphite Lithium Ion Battery Anodes. *Nat. Commun.* **2016**, *7*, 1−11.
(23) Finegan, D. P.; Tudisco, E.; Scheel, M.; Robinson, J. B.; Taiwo, O. O.; Eastwood, D. S.; Lee, P. D.; Michiel, M.; Di; Bay, B.; Hall, S. A.; Hinds, G.; Brett, D. J. L.; Shearing, P. R. Quantifying Bulk Electrode Strain and Material Displacement within Lithium Batteries *via* High-Speed Operando Tomography and Digital Volume Correlation. *Adv. Sci.* **2016**, *3* (3), 1−11.
(24) Eastwood, D. S.; Bradley, R. S.; Tariq, F.; Cooper, S. J.; Taiwo, O. O.; Gelb, J.; Merkle, A.; Brett, D. J. L.; Brandon, N. P.; Withers, P. J.; Lee, P. D.; Shearing, P. R. The Application of Phase Contrast X-Ray Techniques for Imaging Li-Ion Battery Electrodes. *Nucl. Instrum. Methods Phys. Res., Sect. B* **2014**, *324*, 118−123.
(25) Harry, K. J.; Hallinan, D. T.; Parkinson, D. Y.; MacDowell, A. A.; Balsara, N. P. Detection of Subsurface Structures underneath Dendrites Formed on Cycled Lithium Metal Electrodes. *Nat. Mater.* **2014**, *13*, 69−73.
(26) Sun, F.; Zielke, L.; Markötter, H.; Hilger, A.; Zhou, D.; Moroni, R.; Zengerle, R.; Thiele, S.; Banhart, J.; Manke, I. Morphological Evolution of Electrochemically Plated/Stripped Lithium Microstructures Investigated by Synchrotron X-Ray Phase Contrast Tomography. *ACS Nano* **2016**, *10*, 7990−7997.
(27) Shen, F.; Dixit, M. B.; Xiao, X.; Hatzell, K. B. Effect of Pore Connectivity on Li Dendrite Propagation within LLZO Electrolytes Observed with Synchrotron X-Ray Tomography. *ACS Energy Lett.* **2018**, *3*, 1056−1061.
(28) Frenck, L.; Maslyn, J. A.; Loo, W. S.; Parkinson, D. Y.; Balsara, N. P. Impact of Salt Concentration on Nonuniform Lithium Electrodeposition through Rigid Block Copolymer Electrolytes. *ACS Appl. Mater. Interfaces* **2019**, *11*, 47878−47885.
(29) Maslyn, J. A.; Frenck, L.; Loo, W. S.; Parkinson, D. Y.; Balsara, N. P. Extended Cycling through Rigid Block Copolymer Electrolytes Enabled by Reducing Impurities in Lithium Metal Electrodes. *ACS Appl. Energy Mater.* **2019**, *2*, 8197−8206.
(30) Ho, A.; Barai, P.; Maslyn, J. A.; Frenck, L.; Loo, W. S.; Parkinson, D. Y.; Srinivasan, V.; Balsara, N. P. Uncovering the Relationship between Diameter and Height of Electrodeposited Lithium Protrusions in a Rigid Electrolyte. *ACS Appl. Energy Mater.* **2020**, *3*, 9645−9655.
(31) Sun, F.; Osenberg, M.; Dong, K.; Zhou, D.; Hilger, A.; Jafta, C. J.; Risse, S.; Lu, Y.; Markötter, H.; Manke, I. Correlating Morphological Evolution of Li Electrodes with Degrading Electrochemical Performance of Li/LiCoO2 and Li/S Battery Systems: Investigated by Synchrotron X-Ray Phase Contrast Tomography. *ACS Energy Lett.* **2018**, *3*, 356−365.
(32) Pietsch, P.; Wood, V. X-Ray Tomography for Lithium Ion Battery Research: A Practical Guide. *Annu. Rev. Mater. Res.* **2017**, *47*, 451−479.
(33) Bay, B. K.; Smith, T. S.; Fyhrie, D. P.; Saad, M. Digital Volume Correlation: Three-Dimensional Strain Mapping Using X-Ray Tomography. *Exp. Mech.* **1999**, *39*, 217−226.
(34) Bay, B. K. Methods and Applications of Digital Volume Correlation. *J. Strain Anal. Eng. Des.* **2008**, *43* (43), 745−760.
(35) Schweidler, S.; De Biasi, L.; Schiele, A.; Hartmann, P.; Brezesinski, T.; Janek, J. Volume Changes of Graphite Anodes Revisited: A Combined Operando X-Ray Diffraction and *in Situ* Pressure Analysis Study. *J. Phys. Chem. C* **2018**, *122*, 8829−8835.
(36) Dahn, J. R. Phase Diagram of Li_xC_6. *Phys. Rev. B: Condens. Matter Mater. Phys.* **1991**, *44*, 9170−9177.
(37) Louli, A. J.; Li, J.; Trussler, S.; Fell, C. R.; Dahn, J. R. Volume, Pressure and Thickness Evolution of Li-Ion Pouch Cells with Silicon-Composite Negative Electrodes. *J. Electrochem. Soc.* **2017**, *164*, A2689−A2696.
(38) Finegan, D. P.; Vamvakeros, A.; Cao, L.; Tan, C.; Heenan, T. M. M.; Daemi, S. R.; Jacques, S. D. M.; Beale, A. M.; Di Michiel, M.; Smith, K.; Brett, D. J. L.; Shearing, P. R.; Ban, C. Spatially Resolving Lithiation in Silicon−Graphite Composite Electrodes *via* in Situ High-Energy X-Ray Diffraction Computed Tomography. *Nano Lett.* **2019**, *19*, 3811−3820.
(39) Paganin, D.; Mayo, S. C.; Gureyev, T. E.; Miller, P. R.; Wilkins, S. W. Simultaneous Phase and Amplitude Extraction from a Single Defocused Image of a Homogeneous Object. *J. Microsc.* **2002**, *206*, 33−40.
(40) Gursoy, D.; De Carlo, F.; Xiao, X.; Jacobsen, C. TomoPy: A Framework for the Analysis of Synchrotron Tomographic Data. *J. Synchrotron Radiat.* **2014**, *21*, 1188−1193.
(41) Bar-Kochba, E.; Toyjanova, J.; Andrews, E.; Kim, K. S.; Franck, C. A Fast Iterative Digital Volume Correlation Algorithm for Large Deformations. *Exp. Mech.* **2015**, *55*, 261−274.

https://doi.org/10.1021/acsnano.1c02942
ACS Nano XXXX, XXX, XXX−XXX